Progress in PHOTOVOLTAICS

PROGRESS IN PHOTOVOLTAICS: RESEARCH AND APPLICATIONS
Prog. Photovolt: Res. Appl. 2016; **24**:725–734
Published online 6 December 2015 in Wiley Online Library (wileyonlinelibrary.com). DOI: 10.1002/pip.2729

RESEARCH ARTICLE

High efficiency UMG silicon solar cells: impact of compensation on cell parameters

Fiacre Rougieux[1]*, Christian Samundsett[1], Kean Chern Fong[1], Andreas Fell[1], Peiting Zheng[1], Daniel Macdonald[1], Julien Degoulange[2], Roland Einhaus[2] and Maxime Forster[2]

[1] Research School of Engineering, College of Engineering and Computer Science, The Australian National University, Canberra, ACT 2601, Australia
[2] Apollon Solar, France

ABSTRACT

High efficiency solar cells have been fabricated with wafers from an n-type Czochralski grown (Cz) ingot using 100% Upgraded Metallurgical-Grade (UMG) silicon feedstock. The UMG cells fabricated with a passivated emitter and rear totally diffused (PERT) structure have an independently confirmed cell efficiency of 19.8%. This is the highest efficiency reported for a cell based on 100% UMG silicon at the time of publication. The current and power losses are analysed as a function of measured material parameters, including carrier mobility, lifetime and the presence of the boron–oxygen defect. Dopant compensation is shown to reduce both the minority carrier lifetime and mobility, which significantly affects both the current and voltage of the device. Copyright © 2015 John Wiley & Sons, Ltd.

KEYWORDS
silicon; upgraded metallurgical grade; compensation; boron–oxygen; mobility; solar cell

***Correspondence**
F. E. Rougieux, School of Engineering, College of Engineering and Computer Science, The Australian National University, Canberra, ACT 0200, Australia.
E-mail: Fiacre.Rougieux@anu.edu.au

Received 19 May 2015; Revised 4 November 2015; Accepted 4 November 2015

1. INTRODUCTION

Upgraded Metallurgical-Grade (UMG) silicon has raised interest as an alternative material for silicon solar cells [1–7]. UMG silicon is produced using a liquid phase purification of Metallurgical-Grade (MG) silicon, but contains more impurities than electronic-grade (EG, vapour phase purification) silicon, especially shallow acceptors (B, Al) and donors (P). This leads to reduced carrier mobilities and the formation of boron–oxygen (BO) defects in n-type silicon. In p-type UMG silicon the BO defect is known to affect the cell parameters [8,9]. For the desired application of n-type UMG silicon in higher efficiency structures, it is critical to assess the potential impact of the reduced mobility and the presence of the BO defect on the cell parameters. Previous studies have attempted to quantify the detrimental impact of the BO defect and reduced mobility on cell parameters of n-type UMG solar cells; however they were conducted on low efficiency structures (6–15%), and were thus less sensitive to the material properties [10–12].

With the recent advent of higher quality UMG material [13], there is now improved scope for higher efficiency devices. In 2011, comparable cell efficiencies were achieved using p-type multicrystalline silicon with UMG feedstock (18.35%) and feedstock from the Siemens process (18.45%, large-area PERC with full area front emitter) [5]. A switch to n-type Cz UMG silicon allowed for 19% efficient solar cells using a heterojunction design (large area) [6]. This was followed by a 19% efficient n-type Cz UMG solar cell using a simpler homojunction cell process with aluminium emitter (large-area screen printed with full rear emitter and selective front surface diffusion) [7].

In this paper further improvement of n-type solar cells made from 100% UMG Czochralski-grown (Cz) silicon is reported. The high efficiency device also allows accurate analysis of the impact of reduced mobilities and the presence of the BO defect on the cell parameters.

Copyright © 2015 John Wiley & Sons, Ltd.

2. EXPERIMENTAL METHOD

The wafers used in this study were sliced from two monocrystalline n-type silicon ingots. The first group of wafers came from an ingot grown with 100% UMG silicon. The UMG feedstock was produced by FerroPerm in the framework of the PHOTOSIL project, the refinement process consisting of an inductive plasma treatment to reduce the boron concentration followed by an optimized segregation process to remove metals impurities and Phosphorus [14]. Glow discharge mass spectroscopy (GDMS) analysis on the feedstock reveals the presence of boron $[B] = 4.3 \times 10^{16}\,cm^{-3}$, phosphorus $[P] = 1.9 \times 10^{16}\,cm^{-3}$ and aluminium $[Al] = 1 \times 10^{15}\,cm^{-3}$, whilst iron and copper concentration are below their respective detection limits $[Fe] < 1.3 \times 10^{15}\,cm^{-3}$ and $[Cu] < 2.2 \times 10^{14}\,cm^{-3}$. Phosphorus highly doped Silicon was added to the UMG feedstock when the crucible was loaded to obtain a 100% n-type ingot, the total contents of Phosphorus in the final ingot was $1 \times 10^{17}\,cm^{-3}$.

The UMG ingot was grown using the Czochralski process and had a diameter of 6 in and a mass of 5.55 kg. The interstitial oxygen concentration and substitutional carbon concentration were determined through low temperature μFTIR measurements. The oxygen concentration was found to be $[O_i] = 1.1 \times 10^{18}\,cm^{-3}$ at the top of the ingot and $[O_i] = 6.0 \times 10^{17}\,cm^{-3}$ at the bottom of the ingot. The substitutional carbon concentration was found to be $[C_s] = 1.1 \times 10^{17}\,cm^{-3}$ at the top of the ingot and $[C_s] = 6.8 \times 10^{17}\,cm^{-3}$ at the bottom of the ingot. The wafers used for cell fabrication came from the first half of the ingot (fraction solidified = 35%) and were close to the wafers used in the lifetime and mobility study (fraction solidified = 40%). The wafers had a net doping concentration $n_0 = 1.3 \times 10^{16}\,cm^{-3}$ with $[P] = 5.1 \times 10^{16}\,cm^{-3}$ and $[B] = 3.8 \times 10^{16}\,cm^{-3}$. Wafers for determination of the ingot profile came from five positions along the ingot.

The second group of wafers came from an ingot grown with EG silicon using the floating-zone (FZ) process and had a net doping concentration of $n_0 = [P] = 2.0 \times 10^{15}\,cm^{-3}$. Figure 1 shows a schematic diagram of the passivated emitter and rear totally diffused (PERT) solar cell structure used in this study [15]. The cells were $2 \times 2\,cm^2$ in size, with random pyramid texturing on the front surface, and full-area front boron and rear phosphorus diffusions. The boron diffusion was performed at 950 °C and resulted in a sheet resistance of approximately 118 Ω/□. The phosphorus diffusion was performed at 775 °C followed by a 880 °C oxidation and resulted in a sheet resistance of approximately 148 Ω/□. The front surface passivation layer was an Al_2O_3/SiN_x stack, and the rear passivation layer was a single SiN_x film. Al_2O_3 was deposited by atmospheric pressure chemical vapour deposition (APCVD) [16] and SiN_x by plasma-enhanced chemical vapour deposition (PECVD). Front and rear contacts were defined by photolithography followed by thermal evaporation of Cr/Pd/Ag stacks, with subsequent silver electroplating.

Lifetime samples were used to monitor the bulk lifetime throughout the process, and after activation of the BO defect. Minority carrier lifetime measurements were performed using the QSSPC and transient photoconductance method [17] with a Sinton WCT120 system. 100 Ω.cm p-type and n-type wafers were used to measure the recombination parameter J_0 of passivated phosphorus and boron diffusions respectively. The majority carrier mobility was measured on $1 \times 1\,cm^2$ Van der Pauw structures using the Hall effect [18]. Temperature-dependent Hall measurements were conducted using an Ecopia HMS-5000 device equipped with a temperature controlled system cooled with liquid nitrogen. The Hall carrier density n_{0H} and resistivity were measured on Van der Pauw structures between 80 and 350 K [18]. The conductivity carrier density n_0 was then calculated from the Hall carrier density using

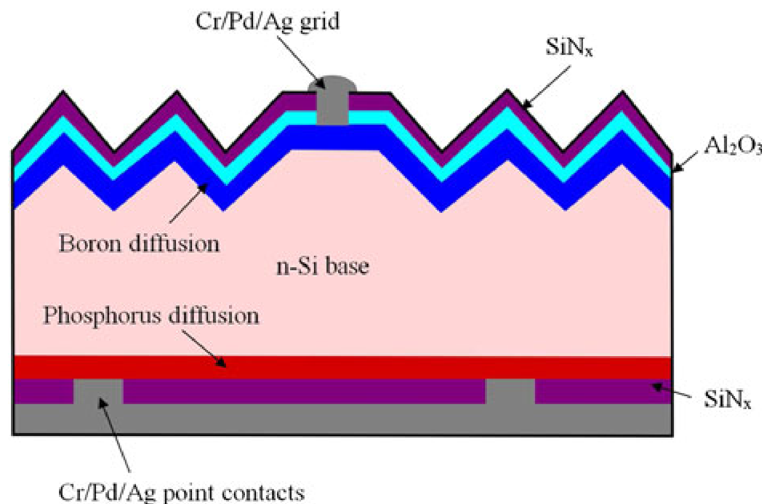

Figure 1. Schematic representation of UMG silicon solar cells with full front boron and rear phosphorus diffusion, Al_2O_3/SiN_x stack at the front, SiN_x at the rear and Cr/Pd/Ag stack at the front and rear.

Prog. Photovolt: Res. Appl. 2016; **24**:725–734 © 2015 John Wiley & Sons, Ltd.
DOI: 10.1002/pip

the *T*-dependent parametrization of the Hall factor r_H provided by Ohta and Sakata $n_0 = r_H \times n_{0,H}$ [19]. In the FZ EG cell, both majority and minority carrier mobility were simulated using Klaassen's model [20,21]. The minority carrier mobility in the UMG wafers was simulated using a modified version of Klaassen's model adapted for compensated silicon [22]. Dark *I–V* measurements were performed using a Keithley 2400 source meter, the TLM measurements using a four point probe and the Suns-Voc measurements using a Suns-Voc from Sinton Instruments [23].

3. UMG MATERIAL PARAMETERS

3.1. Lifetime and BO defect

Three UMG control samples were prepared to investigate the impact of high temperature processing on the minority carrier lifetime. Sample 1 was left as-grown, sample 2 underwent the boron diffusion and sample 3 both the boron and phosphorus diffusions. All samples were then etched back to remove diffused layers and passivated with SiN_X. The minority carrier lifetime also degrades in n-type UMG silicon because of the formation of the BO defect [24–28]. In order to investigate the effect of the BO defect, sample 3 was subsequently illuminated for different lengths of time (15 min, 90 min and 100 h at 26 mW cm^{-2}). Lifetime measurements were taken using a Sinton WTC-120 and are presented in Figure 2.

Both thermal diffusion processes were found to degrade the lifetime. Bulk lifetime degradation is known to occur in n-type Cz silicon after boron diffusion and is usually associated with the nucleation and growth of recombination active oxygen precipitates [29,30] during the 900 °C–950 °C diffusion step [31–33]. However, in our case, it is clear that this degradation also occurs for the FZ wafers where no oxygen precipitates should nucleate. Also note that the lifetime does not increase after the phosphorus diffusion which suggests that fast diffusing metallic impurities may not be responsible for the lifetime degradation. Hence, it is possible that the degradation observed here is not because of oxygen precipitates or metallic impurities but rather to dislocations created during boron diffusion as observed by others [34]. In the UMG material, light-induced degradation also led to a further reduction of the lifetime from 115 µs to 62 µs (at $\Delta p = 1 \times 10^{15}$ cm^{-3}) because of the formation of the BO defect.

3.2. Majority and minority carrier mobility

In order to determine the dopant concentration in the CZ UMG cells we used the initial boron and phosphorus concentration present in the feedstock (measured by GDMS) together with the concentration of added phosphorus as a first guess [35]. We then used Scheil's equation, with segregation coefficient of $k_B = 0.8$ for boron, $k_P = 0.35$ for phosphorus [36] to obtain the dopant profile of the ingot. To validate (and obtain a more precise determination of) the dopant concentration in the UMG cells (fs = 35%) we performed temperature-dependent Hall measurements on wafers at fs = 40%. We then simulated the temperature dependence of the net doping and kept $[P^+] - [B^-]$ constant whilst changing [P] and [B] together until the simulated and measured temperature dependence of the net doping fit. Figure 3 shows the measured temperature-dependent Hall measurements, together with the fit to obtain separately the boron and phosphorus concentration.

During this procedure we also take into account the incomplete ionization of phosphorus [37,38] (B is fully ionized in this n-type ingot). We also validated our measurement with measurement of the net doping along the ingot.

Dopant compensation is known to decrease both the minority and majority carrier mobility [25,38–46]. Table I shows the majority and minority carrier mobility of the UMG and EG cells. The UMG Cz cells have majority carrier concentration of $n_0 = [P^+] - [B^-] = 1.3 \times 10^{16}$ cm^{-3}

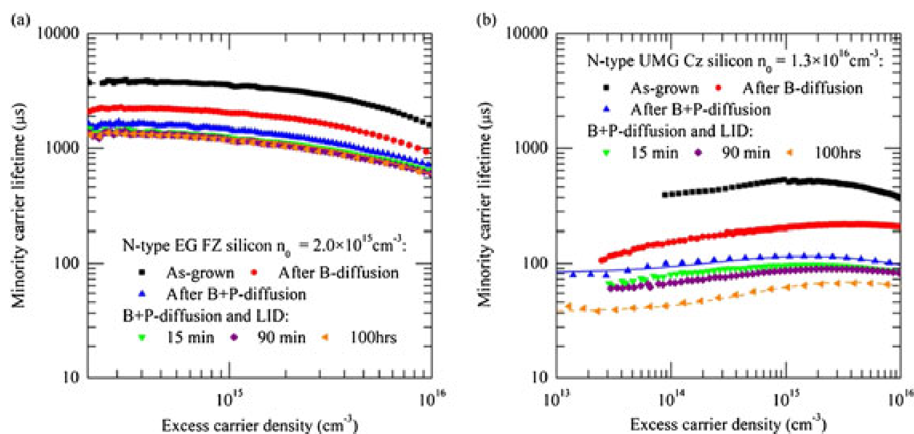

Figure 2. Measured injection-dependent minority carrier lifetime (a) for the n-type EG FZ wafers and (b) the n-type UMG Cz silicon wafers in as-grown state, after boron diffusion, phosphorus diffusion and after different lengths of time under illumination, 15 min, 90 min and 100 h at 26 mW cm^{-2}.

DOI: 10.1002/pip

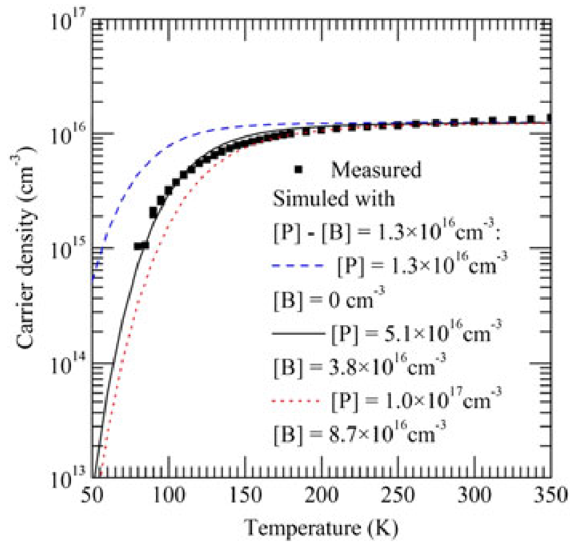

Figure 3. Temperature dependence of the carrier density in the UMG silicon sample at a fraction solidified of 40%. Black square represent the measured Hall data. Solid lines are calculated using a constant carrier density at 300 K ($n_0 = [P^+] - [B^-] = 1.3 \times 10^{16}\,cm^{-3}$) and varying together the phosphorus and boron concentration.

whilst the electronic grade (EG) float-zone (FZ) silicon cells have majority carrier concentration of $n_0 = [P^+] = 2.0 \times 10^{15}\,cm^{-3}$.

In the UMG wafers, the measured majority carrier mobility of $837\,cm^2\,V^{-1}\,s^{-1}$ is significantly lower than the expected value of $1170\,cm^2\,V^{-1}\,s^{-1}$ in uncompensated silicon of comparable net doping concentration ($n_0 = 1.3 \times 10^{16}\,cm^{-3}$). This is because of the presence of additional dopants (with a total concentration $8.9 \times 10^{16}\,cm^{-3}$), which is shown to have an impact on resistive losses in the devices, as discussed in section 5.3 below. The diffusion length is calculated from the measured minority carrier bulk lifetime and simulated minority carrier mobility. The reduced minority carrier mobility of $317\,cm^2\,V^{-1}\,s^{-1}$ has a direct impact on the diffusion length and will impact the device current, as shown in section 5.3 below.

4. CELL RESULTS

Independently measured (at Fraunhofer CalLab) light *I–V* characteristic of the best n-type UMG Cz cell and the best EG FZ cell confirms an efficiency of 19.8% and 21.3% respectively. The cells are measured after light-induced degradation. The average efficiency for the n-type UMG Cz cell (four cells) and the EG FZ cell (four cells) was 19.4% and 21.0% (in-house measurements). The light *I–V* of the measured cells are plotted in Figure 4a along with simulated *I–V* curves (to be discussed further in section 5.3) and details of the extracted parameters are also presented in Table II. When compared to the EG cell, the UMG Cz cell efficiency is reduced by 1.5% absolute, with a loss of $1.6\,mA\,cm^{-2}$ in short-circuit current and a loss of 16 mV in open circuit voltage. The difference in FF between the UMG and EG cells is relatively small. The loss in open circuit voltage reveals the lower minority carrier lifetime of the UMG material. Even though the net dopant density is twice that of the control cells, it is not sufficient to compensate for the lower lifetime of the UMG material. The open-circuit voltage reduction would be more pronounced when compared to a FZ cell with an identical net doping concentration (assuming similar lifetime in the FZ wafer).

The series resistance at MPP (R_{S_MPP}) was extracted by comparing the Suns-V_{OC} measurements with the light *I–V* measurements [47]. The series resistance remains unaffected by the UMG material. As will be shown below this is because the series resistance is dominated by resistive loss other than bulk carrier transport (e.g. front and rear contacts and front diffusion). Dark *I–V* measurements for the UMG Cz and EG FZ cells were fitted to an equivalent circuit model which allows extraction of the shunt resistance (R_{SH}) [48]. The results indicated that shunt resistance is sufficiently high to have a negligible impact on FF for both the UMG Cz and FZ EG cells. Results of extracted R_{SH} and R_s are also included in Table II.

Figure 4b shows the measured and simulated internal quantum efficiency (IQE) of the UMG Cz cell and the EG FZ cell. Details of the simulated IQE are presented in section 5.3. Note that we disregard the effect of escape reflectance R_{escape} and the effect of front film absorption in the calculation of the IQE, meaning $IQE = EQE/(1 - R_{front})$ [49]. All of the current losses are in the high wavelength regions. This is mainly because of the lower diffusion length of the UMG material leading to a loss of photo-generated carriers in the bulk of the material. This comes from contributions of the lower lifetime and also the lower mobility, as shown in section 5.3. The other contribution is because of the thicker wafers used for the control cells. The impact of the UMG material properties on the cell parameters will be discussed in more detail in section 5.3.

Table I. INet doping n_0, thickness W, minority carrier lifetime τ, majority carrier mobility μ_n, minority carrier mobility μ_p and diffusion length L_p in the UMG and EG wafers after processing and activation of the BO defect. All quantities are measured except the minority carrier mobility which is simulated.

Cell	[P]	[B]	n_0 (cm^{-3})	W (μm)	τ (μs) (at $\Delta n = 1 \times 10^{15}\,cm^{-3}$)	μ_n ($cm^2\,V^{-1}\,s^{-1}$)	μ_p ($cm^2\,V^{-1}\,s^{-1}$)	L_p (μm)
UMG Cz	5.1×10^{16}	3.8×10^{16}	1.3×10^{16}	150	62	837	317[a]	224
EG FZ	2.0×10^{15}	—	2.0×10^{15}	280	1160	1348[a]	455[a]	1164

[a]Simulated value.

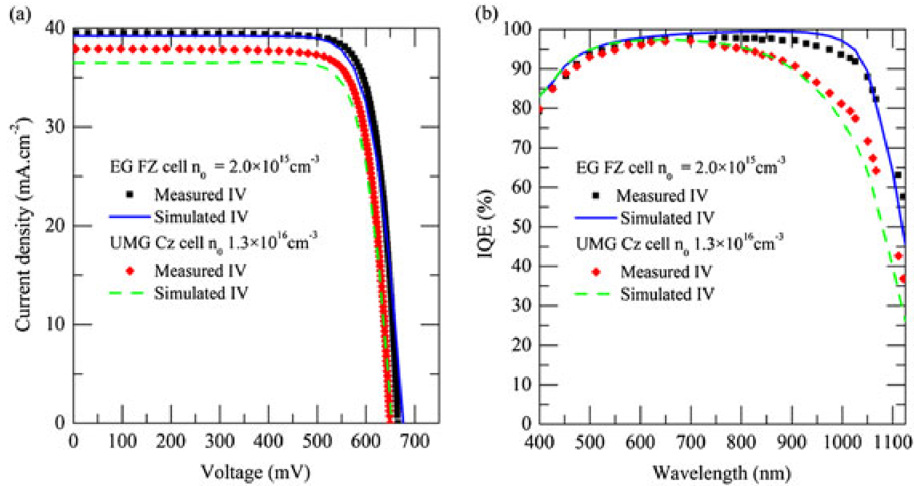

Figure 4. Measured and simulated (a) *I–V* curve and (b) IQE for the FZ EG and UMG Cz cells. *I–V* curve and EQE were independently measured at CalLab.

Table II. IIUMG and EG cell results where J_{SC}, V_{OC}, FF and η are independently measured at Fraunhofer CalLab; pFF, R_S and R_{SH} are in-house measurements.

Cell	n_0 (cm^{-3})	J_{sc} (mA cm^{-2})	V_{OC} (mV)	FF (%)	pFF (%)	R_{SH} (Ω cm^{-2})	$R_{s\ MPP}$ (Ω cm^{-2})	η (%)
UMG Cz	1.3×10^{16}	37.9	649	80.3	81.8	1.0×10^4	0.28	19.8
EG FZ	2.0×10^{15}	39.5	665	81.2	82.4	3.0×10^4	0.32	21.3

5. SIMULATION OF THE CELLS

5.1. Optics

As shown in the IQE data above, the main current losses are in the infrared region. It is therefore critical to accurately model the wafer optical properties. The optics is modelled using the wafer ray tracer v1.6.4 software from PV Lighthouse [50]. We model the front texture with a Al_2O_3/SiN_x stack with thicknesses of 5 nm and 55 nm respectively, matching our reflectance measurements, and a rear reflector, 60% Lambertian fraction, with 92% reflectance. The rear reflectance is adjusted until the escape reflectance matches the measured reflectance. Figure 5 shows the measured and simulated reflectance of the cell structure without the influence of front finger reflectance. The wafer ray tracer also outputs pathlength enhancement that is then used in Quokka (a 3D semiconductor simulation tool) to calculate the generation profile in the devices [51].

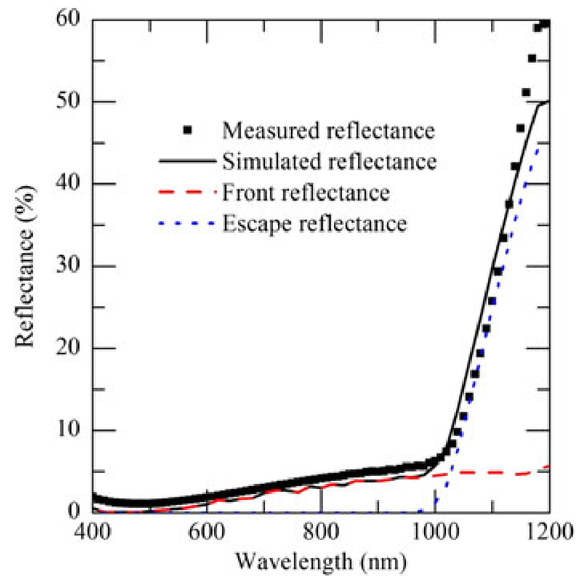

Figure 5. Measured and simulated reflectance of the cell structure without the front fingers. The escape reflectance is only significant at wavelength above 1000 nm.

5.2. Electronic properties

Modelling of the device performance is conducted using Quokka 3D modelling [52]. This programme uses the conductive boundary approximation and thus we use measured values of the front and rear recombination parameters J_0 to account for the recombination at these boundaries [52]. Table III shows the parameters used in the Quokka simulation. Sheet resistance, contact resistance and $J_{0passivated}$ parameters are measured whilst $J_{0,contacted}$ are taken from typical values for a 150 Ω/□ phosphorus diffusion [53] and for a 120 Ω/□ boron diffusion [54]. The conductive boundary approximation requires the

Table III. IIISimulation parameters used in the Quokka simulation of the cells.

Side	Properties	Value
Front	Sheet R	118 Ω/□
	$R_{contact}$	2.4 mΩ cm^2
	$J_{0,passivated}$	35 fA cm^{-2}
	$J_{0,contacted}$	1800 fA cm^{-2}
	Contact width	10-μm fingers
	Contact spacing	1200 μm
Rear	Sheet R	148 Ω/□
	$R_{contact}$	0.6 mΩ cm^2
	$J_{0,passivated}$	30 fA cm^{-2}
	$J_{0,contacted}$	1100 fA cm^{-2}
	Contact width	30-μm dots
	Contact spacing	300 μm

collection efficiency of the emitter as an independent input, which we set to a constant spectrum-average value of 81% corresponding to the IQE value at 400 nm. Note that this collection efficiency includes front film absorption (which is significant at 400 nm)—this means the actual electrical collection efficiency is higher. The front collection efficiency only impacts the low wavelength part of the spectrum; as the region of interest in our study is the high wavelength range of the IQE this has a minimal impact on our analysis.

As the as-grown bulk lifetime is not representative of the final bulk lifetime, the bulk lifetime post high temperature processing is used in the modelling. The minority carrier bulk lifetime is modelled in Quokka using two defects and a J_{0SiN} (measured separately) fitted to the measured lifetime for the EG FZ and UMG CZ test structures. We use the bulk lifetime post process and BO activation (100-h illumination) to model the influence of the BO defect on the efficiency. Table IV shows the SRH parameters extracted from the lifetime test structures and used in the simulation of the cells. The mobility is modelled using Klaassen's model for the EG FZ cell and modelled using measured and simulated values (for majority and minority carrier respectively) for the UMG Cz cell.

5.3. Simulation results

Simulation of the *I–V* characteristics of the cells is shown in Figure 4. Whilst lifetime and recombination parameters J_0 are measured with high accuracies, the simulation of the optics and the measurements of the contact resistance are two important sources of inaccuracies in the simulation. The relatively good agreement between the measured and simulated *I–V* curve and IQE characteristics validates our simulations (the short circuit current is underestimated in the UMG cells). All cell parameters such as contact

Table IV. IVSimulation parameters used for the different scenarios.

Scenario	W (μm)	n_0 (cm^{-3})	$E_C - E_T$	$\sigma_p \times N_t$	σ_n/σ_p	μ_n	μ_p
EG material	280	2.0×10^{15}	0.5 eV 0.95 eV	5.2×10^{-5} cm^{-1} 8.0×10^{-4} cm^{-1}	100 0.37	1348	455
Thickness and doping adjusted	150	1×10^{16}	0.5 eV 0.95 eV	5.2×10^{-5} cm^{-1} 8.0×10^{-4} cm^{-1}	100 0.37	1348	455
+ reduced mobility	150	1×10^{16}	0.5 eV 0.95 eV	5.2×10^{-5} cm^{-1} 8.0×10^{-4} cm^{-1}	100 0.37	837	317
+ reduced lifetime	150	1×10^{16}	0.5 eV 1 eV	4.5×10^{-4} cm^{-1} 1.3×10^{-3} cm^{-1}	0.02 30	837	317
+ activated BO defect	150	1×10^{16}	0.5 eV 1 eV	1.5×10^{-3} cm^{-1} 1.9×10^{-3} cm^{-1}	0.04 30	837	317

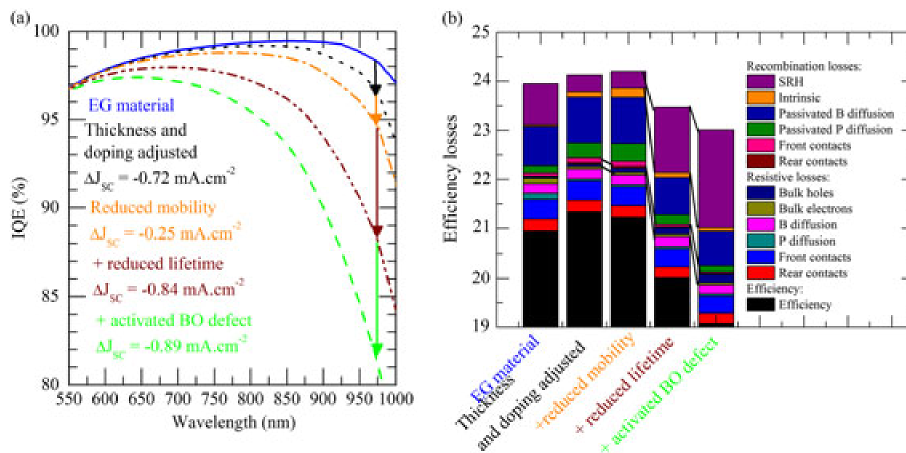

Figure 6. Simulated influence of the reduced lifetime, mobility and BO defect on the (a) short circuit current losses in the IQE curve and (b) power losses using a free energy loss analysis (FELA) in the UMG Cz cells, for ease of reading optics losses are not presented. The solid line "EG material" and dashed line "+activated BO defect" correspond to the simulations in Figure 4.

Prog. Photovolt: Res. Appl. 2016; **24**:725–734 © 2015 John Wiley & Sons, Ltd.
DOI: 10.1002/pip

fraction, contact diameters, J_0 and R_{sheet} have been kept constant between the EG and UMG simulation. Only the lifetime, the mobility, thickness and net doping have changed. The only wavelength region where the IQE simulation differs is in the infrared.

We then use this simulation as a basis to explore the influence of both lower mobility and lower lifetime on the short circuit current and efficiency of the UMG cells. For this we use our measurements of the lifetime and mobility on test structures as input parameters for the simulation. To allow for a meaningful comparison between the UMG cells Table IV shows the parameters used for each scenario.

Figure 6a shows the simulated influence of reduced lifetime, mobility and BO defect on the short circuit current losses in the IQE curve. The dash-dot green curve in Figure 6a is identical to the dashed green curve showing the IQE of the UMG sample in Figure 4b. The measured loss of $1.6\,mA\,cm^{-2}$ shown in Table II can be explained by $0.72\,mA\,cm^{-2}$ reduction in short-circuit current because of a thinner wafer coupled with a $0.25\,mA\,cm^{-2}$ reduction because of the reduced mobility, a further $0.84\,mA\,cm^{-2}$ because of a combination of reduced mobility and lifetime and an additional $0.89\,mA\,cm^{-2}$ because of a combination of reduced mobility, lifetime and activated BO defect. Note that the order in which we determine the impact of each loss mechanism is important. For instance, if we take into account the loss because of mobility last, its net effect is made worse by the lower lifetime. We decided to order the losses from the hardest to remove (reduced mobility) to the easiest to removed (BO defect).

Figure 6b shows the influence of reduced lifetime, mobility and BO defect on the recombination and resistive losses at MPP. Optical losses are identical for all scenarios except the first one and therefore not displayed here. The power losses were determined via a Free Energy Loss Analysis (FELA) [55]. The advantage of FELA is that both resistive, recombination and optical losses can be expressed as a percentage of the efficiency [56]. This is especially important for our analysis as a current loss analysis will miss the resistive losses because of lower mobility in the UMG material.

Whereas all the simulated cells have the same thickness and optical properties, the FELA contributions do not add up to the same efficiency value. They instead add up to the volume integral of photogeneration rate multiplied by the splitting of the quasi-Fermi levels at MPP. This means that whilst the photogeneration current in cells with identical optical properties is the same, cells with reduced lifetime have smaller quasi-Fermi level splitting (lower excess carrier densities at MPP) and hence lower FELA contributions. For the simulation with lower mobility on the other hand, electrons and holes are harder to extract and hence tend to accumulate in the bulk, leading to a slightly greater splitting of the quasi-Fermi levels. Whilst the absolute loss values need therefore be interpreted with care, they are still useful to assess the impact of incremental changes to cell design.

Power losses because of increased recombination are the most significant. SRH recombination losses increase from 0.30% to 1.3% with reduced lifetime and to 1.9% with the activated BO defect. Power loss because of increased bulk resistive losses are significantly less important and account for losses of 0.10% to 0.14% with reduced mobility and 0.23% with reduced mobility, reduced lifetime and activated BO defect. Once again one cannot decouple the conductivity and lifetime reduction. When the BO defect is present, the lower minority hole concentration leads to a lower hole conductivity that is amplified by the lower minority hole mobility ($\sigma_p = q\Delta p\mu_p$).

6. CONCLUSION

We have demonstrated the possibility of using n-type UMG monocrystalline silicon to manufacture solar cells with efficiency close to 20%. Compared to control cells on EG wafers, a 1.5% drop in efficiency is seen because of the lower bulk lifetime and mobility of UMG silicon. The lower lifetime and diffusion length of the UMG material reduced the V_{OC} by 16 mV and J_{SC} by $1.6\,mA\,cm^{-2}$ whilst other parameters such as R_S and R_{SH} are not significantly affected. Whilst the reduced mobility alone has a small impact on the efficiency it significantly decreases the bulk collection efficiency when combined with lower lifetimes. Our simulations indicate that implementing strategies to remove the BO defect (for, e.g. advanced hydrogenation processes) can lead to efficiencies above 20% in UMG silicon using this PERT structure. Efficiencies of 21% can potentially be reached by removing other defects present in UMG materials, e.g. by advanced UMG purification or extended gettering during solar cell processing. Still higher efficiency could be reached by removing the compensating boron entirely from the feedstock, to avoid the mobility reduction in the material. To our knowledge, an efficiency of 19.8% for a 100% UMG silicon solar cell is the highest efficiency reported to date.

ACKNOWLEDGEMENTS

This work was supported by the Australian Renewable Energy Agency (ARENA) through their postdoctoral fellowship programme and through the Australian Centre for Advanced Photovoltaics (ACAP).

REFERENCES

1. Yuge N, Abe M, Hanazawa K, Baba H, Nakamura N, Kato Y, Sakaguchi Y, Hiwasa S, Aratani F. Purification of metallurgical-grade silicon up to solar grade. *Progress in Photovoltaics: Research and Applications* 2001; **9**: 203–209.

2. Kohler D, Raabe B, Braun S, Seren S, Hahn G. *Upgraded Metallurgical Grade Silicon Solar Cells: A Detailed Material Analysis*. 2009.
3. Ounadjela K, Bloss A. *New Metallization Technique for 6 MW Pilot Production of Multicrystalline Solar Cells Using Upgraded Metallurgical Grade Silicon*. CaliSolar inc: Sunnyvale, 2010.
4. Kraiem J, Drevet B, Cocco F, Enjalbert N, Dubois S, Camel D, Grosset-Bourbange D, Pelletier D, Margaria T, Einhaus R. "High performance solar cells made from 100% UMG silicon obtained via the PHOTOSIL process", in *Photovoltaic Specialists Conference* (*PVSC*), *2010 35th IEEE*, 2010, 001427–001431.
5. Engelhart P, Wendt J, Schulze A, Klenke C, Mohr A, Petter K, Stenzel F, Hornlein S, Kauert M, Junghanel M, Barkenfelt B, Schmidt S, Rychtarik D, Fischer M, Muller JW, Wawer P. R and D pilot line production of multi-crystalline Si solar cells exceeding cell efficiencies of 18%. *Energy Procedia* 2011; **8**: 313–317.
6. Degoulange J, Einhaus R, Kraiem J, Cocco F, Grosset D, Andrault Y, Pappet P. *High Efficiency Heterojunction Solar Cells on Highly Purified n-Type UMG Cz Wafers*ed. 2012.
7. Schiele Y, Wilking S, Book F, Wiedenmann T, Hahn G. Record efficiency of PhosTop solar cells from n-type Cz UMG silicon wafers. *Energy Procedia* 2013; **38**: 459–466.
8. Forster M, Wagner P, Degoulange J, Einhaus R, Galbiati G, Rougieux FE, Cuevas A, Fourmond E. Impact of compensation on the boron and oxygen-related degradation of upgraded metallurgical-grade silicon solar cells. Proceedings of the 24th European Photovoltaic Solar Energy Conference, Hamburg, Germany (WIP-Renewable Energies, Munich, Germany) *Solar Energy Materials and Solar Cells* 2014; **120**: 390–395.
9. Tanay F, Dubois S, Enjalbert N, Veirman J. Low temperature-coefficient for solar cells processed from solar-grade silicon purified by metallurgical route. *Progress in Photovoltaics: Research and Applications* 2011; **19**: 966–972.
10. Xiao C, Yang D, Yu X, Wang R, Que D. Analysis of the photovoltaic properties of n-type compensated silicon solar cells with the Al-alloyed emitter. *Journal of Alloys and Compounds* 2013; **561**: 28–32 6/5/.
11. Schutz-Kuchly T, Dubois S, Veirman J, Veschetti Y, Heslinga D, Palais O. Light-induced degradation in compensated n-type Czochralski silicon solar cells. *Physica Status Solidi (a)* 2010; **208**: 572–575.
12. Schutz-Kuchly T, Sanzone V, Veschetti Y. N-type solar-grade silicon purified via the metallurgical route: characterisation and fabrication of solar cells. *Progress in Photovoltaics: Research and Applications* 2013; **21**: 1214–1221.
13. Forster M, Fourmond E, Einhaus R, Lauvray H, Kraiem J, Lemiti M. Ga co-doping in Cz-grown silicon ingots to overcome limitations of B and P compensated silicon feedstock for PV applications. *Physica Status Solidi C* 2011; **8**: 678–681.
14. Cocco F, Grosset-Bourbange D, Rivat P, Quost G, Degoulange J, Einhaus R, Forster M, Colin H. Photosil UMG silicon: industrial evaluation by multi-c p-type ingots and solar cells. In *Proceedings of the 28th European Photovoltaic Solar Energy Conference*, Paris, France. WIP-Renewable Energies: Munich, Germany, 2013.
15. Zhao J , Wang A, Dai X, Green MA , Wenham SR. Improvements in silicon solar cell performance. In *Photovoltaic Specialists Conference*, *1991.*, *Conference Record of the Twenty Second IEEE*, **1**, 1991; 399–402.
16. Black LE, McIntosh KR. Surface passivation of c-Si by atmospheric pressure chemical vapor deposition of Al_2O_3. *Applied Physics Letters* 2012; **100**: 202107.
17. Sinton RA, Cuevas A. Contactless determination of current–voltage characteristics and minority-carrier lifetimes in semiconductors from quasi-steady-state photoconductance data. *Applied Physics Letters* 1996; **69**: 2510–2512.
18. Van der Pauw L. A method of measuring the Resistivity and Hall coefficient on lamellae of arbitrary shape. *Philips Technical Review* 1958; **20**: 221–224.
19. Ohta E, Sakata M. Temperature dependence of Hall factor in low-compensated n-type silicon. *Japanese Journal of Applied Physics* 1978; **17**: 1795–1804.
20. Klaassen DBM. A unified mobility model for device simulation—I. Model equations and concentration dependence. *Solid-State Electronics* 1992; **35**: 953–959.
21. Klaassen DBM. A unified mobility model for device simulation—II. Temperature dependence of carrier mobility and lifetime. *Solid-State Electronics* 1992; **35**: 961–967.
22. Schindler F, Forster M, Broisch J, Schön J, Giesecke J, Rein S, Warta W, Schubert MC. Towards a unified low-field model for carrier mobilities in crystalline silicon. *Solar Energy Materials and Solar Cells* 2014; **131**: 92–99 12//.
23. Sinton R, Cuevas A. A quasi-steady-state open-circuit voltage method for solar cell characterization. In *Proceedings of the 24th European Photovoltaic Solar Energy Conference*, Hamburg, Germany. WIP-Renewable Energies: Munich, Germany, 2000.
24. Schutz-Kuchly T, Veirman J, Dubois S, Heslinga DR. Light-induced-degradation effects in boron–phosphorus compensated n-type Czochralski silicon. *Applied Physics Letters* 2010; **96**: 093505.
25. Lim B, Rougieux F, Macdonald D, Bothe K, Schmidt J. Generation and annihilation of boron—oxygen-related recombination centers in compensated p- and

n-type silicon. *Journal of Applied Physics* 2010; **108**: 103722.
26. Rougieux FE, Lim B, Schmidt J, Forster M, Macdonald D, Cuevas A. Influence of net doping, excess carrier density and annealing on the boron oxygen related defect density in compensated n-article silicon. *Journal of Applied Physics* 2011; **110**: 063708.
27. Rougieux FE, Forster M, Macdonald D, Cuevas A, Lim B, Schmidt J. Recombination activity and impact of the boron–oxygen-related defect in compensated N-type silicon. *Photovoltaics, IEEE Journal of* 2011; **1**: 54–58.
28. Geilker J, Kwapil W, Rein S. Light-induced degradation in compensated p- and n-type Czochralski silicon wafers. *Journal of Applied Physics* 2011; **109**: 053718.
29. Murphy JD, Bothe K, Olmo M, Voronkov VV, Falster RJ. The effect of oxide precipitates on minority carrier lifetime in p-type silicon. *Journal of Applied Physics* 2011; **110**: 053713.
30. Murphy JD, Bothe K, Krain R, Voronkov VV, Falster RJ. Parameterisation of injection-dependent lifetime measurements in semiconductors in terms of Shockley–Read–Hall statistics: an application to oxide precipitates in silicon. *Journal of Applied Physics* 2012; **111**: 113709.
31. Singh S, Debucquoy M, Wostyn K, Cornagliotti E, O'Sullivan B, Posthuma N, Poortmans J. n-Type silicon wafer screening for IBC solar cells by different thermal treatments. In *Proceedings of the 28th European Photovoltaic Solar Energy Conference*, (WIP-Renewable Energies, Munich, Germany) Paris, France, 2013.
32. Sopori B, Hao-Chih Y, Devayajanam S, Basnyat P, LaSalvia V, Norman A, Page M, Nemeth B, Stradins P. Bulk defect generation during B-diffusion and oxidation of CZ wafers: mechanism for degrading solar cell performance. In *Photovoltaic Specialist Conference* (*PVSC*), *2014 IEEE 40th*, 2014, pp. 0719–0723.
33. Walter D, Lim B, Falster R, Binns MJ, Schmidt J. Understanding lifetime degradation in Czochralski-grown N-type silicon after high-temperature processing. In *Proceedings of the 28th European Photovoltaic Solar Energy Conference*, Paris, France. WIP-Renewable Energies: Munich, Germany, 2013.
34. Cousins PJ, Cotter JE. The influence of diffusion-induced dislocations on high efficiency silicon solar cells. *Electron Devices, IEEE Transactions on* 2006; **53**: 457–464.
35. Scheil E. Bemerkungen zur schichtkristallbildung. *Zeitschrift Metallkiunde* 1942; **34**: 70.
36. Trumbore FA. Solid solubilities of impurity elements in germanium and silicon. *The Bell System Technichal Journal* 1960; **39**: 205–233.
37. Altermatt PP, Schenk A, Heiser G. A simulation model for the density of states and for incomplete ionization in crystalline silicon. I. Establishing the model in Si: P. *Journal of Applied Physics* 2006; **100**: 113714.
38. Forster M, Cuevas A, Fourmond E, Rougieux FE, Lemiti M. Impact of incomplete ionization of dopants on the electrical properties of compensated p-type silicon. *Journal of Applied Physics* 2012; **111**: 043701.
39. Rougieux FE, Macdonald D, Cuevas A, Ruffell S, Schmidt J, Lim B, Knights AP. Electron and hole mobility reduction and Hall factor in phosphorus-compensated p-type silicon. *Journal of Applied Physics* 2010; **108**: 013706.
40. Rougieux FE, Macdonald D, Cuevas A. Transport properties of p-type compensated silicon at room temperature. *Progress in Photovoltaics: Research and Applications* 2011; **19**: 787–793.
41. Veirman J, Dubois S, Enjalbert N, Garandet JP, Heslinga DR, Lemiti M. Hall mobility reduction in single-crystalline silicon gradually compensated by thermal donors activation. *Solid-State Electronics* 2010; **54**: 671–674.
42. Veirman J, Dubois S, Enjalbert N, Garandet J-P, Lemiti M. Electronic properties of highly-doped and compensated solar-grade silicon wafers and solar cells. *Journal of Applied Physics* 2011; **109**: 103711.
43. Lim B, Wolf M, Schmidt J. Carrier mobilities in multicrystalline silicon wafers made from UMG-Si. *Physica Status Solidi C* 2011; **235**: 835–838.
44. Fourmond E, Forster M, Einhaus R, Lauvray H, Kraiem J, Lemiti M. Electrical properties of boron, phosphorus and gallium co-doped silicon. *Energy Procedia* 2011; **8**: 349–354.
45. Schindler F, Geilker J, Kwapil G, Giesecke J, Schubert MC, Warta W. *Conductivity Mobility and Hall Mobility in Compensated Multicrystalline Silicon*, Proceedings of the 25th European Photovoltaic Solar Energy Conference, Valencia, Spain. WIP-Renewable Energies: Munich, Germany, ed. 2010.
46. Schindler F, Schubert MC, Kimmerle A, Broisch J, Rein S, Kwapil W, Warta W. Modeling majority carrier mobility in compensated crystalline silicon for solar cells. *Solar Energy Materials and Solar Cells* 2012; **106**: 31–36.
47. Aberle AG, Wenham SR, Green MA. A new method for accurate measurements of the lumped series resistance of solar cells. In *Photovoltaic Specialists Conference*, *1993*., *Conference Record of the Twenty Third IEEE*, 1993, pp. 133–139.
48. McIntosh KR. Lumps, humps and bumps: three detrimental effects in the current–voltage curve of a silicon solar cell, PhD thesis, 2001.

49. Basore PA. Extended spectral analysis of internal quantum efficiency. In *Photovoltaic Specialists Conference*, *1993*., *Conference Record of the Twenty Third IEEE*, 1993, 147–152.
50. PVLightouse, http://www.pvlighthouse.com.au/, 2015.
51. Fell A, McIntosh KR. Deriving the generation profile for silicon solar cell modeling from lumped optical parameters. In *Photovoltaic Specialists Conference, 1993., New Orleans, USA*. *Conference Record of the Forty Second IEEE*, ed. 2015; Submitted.
52. Fell A. A free and fast three-dimensional/two-dimensional solar cell simulator featuring conductive boundary and quasi-neutrality approximations. *Electron Devices, IEEE Transactions on* 2013; **60**: 733–738.
53. Cuevas A, Basore PA, Giroult-Matlakowski G, Dubois C. Surface recombination velocity of highly doped n-type silicon. *Journal of Applied Physics* 1996; **80**: 3370–3375.
54. Benick J, Hoex B, van de Sanden MCM, Kessels WMM, Schultz O, Glunz SW. High efficiency n-type Si solar cells on Al_2O_3-passivated boron emitters. *Applied Physics Letters* 2008; **92**: 253504.
55. Brendel R, Dreissigacker S, Harder N-P, Altermatt PP. Theory of analyzing free energy losses in solar cells. *Applied Physics Letters* 2008; **93**: 173503.
56. Franklin E, Fong K, McIntosh K, Fell A, Blakers A, Kho T, Walter D, Wang D, Zin N, Stocks M, Wang E-C, Grant N, Wan Y, Yang Y, Zhang X, Feng Z, Verlinden PJ. Design, fabrication and characterisation of a 24.4% efficient interdigitated back contact solar cell. *Progress in Photovoltaics: Research and Applications* 2014.

Prog. Photovolt: Res. Appl. 2016; **24**:725–734 © 2015 John Wiley & Sons, Ltd.
DOI: 10.1002/pip